

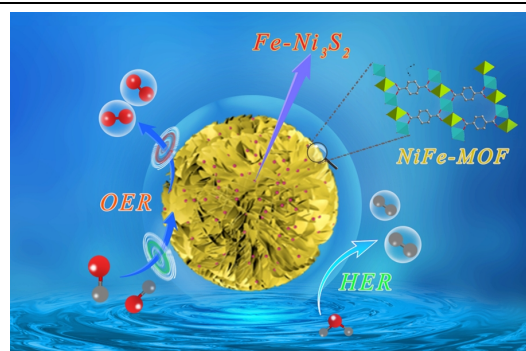
# Coupling of NiFe-Based Metal-Organic Framework Nanosheet Arrays with Embedded Fe-Ni<sub>3</sub>S<sub>2</sub> Clusters as Efficient Bifunctional Electrocatalysts for Overall Water Splitting

Xianbiao Hou<sup>1#</sup>, Tianyuan Jiang<sup>1#</sup>, Xiujuan Xu<sup>1</sup>, Xingkun Wang<sup>1</sup>, Jian Zhou<sup>1</sup>, Huimin Xie<sup>1</sup>, Zhicheng Liu<sup>1</sup>, Lei Chu<sup>1\*</sup> and Minghua Huang<sup>1\*</sup>

<sup>1</sup>School of Materials Science and Engineering, Ocean University of China, Qingdao 266100, China

**ABSTRACT** Developing highly efficient, easy-to-make and cost-effective bifunctional electrocatalysts for water splitting with lower cell voltages is crucial to producing massive hydrogen fuel. In response, the coupled hierarchical Ni/Fe-based MOF nanosheet arrays with embedded metal sulfide nanoclusters onto nickel foam skeleton (denoted as Fe-Ni<sub>3</sub>S<sub>2</sub>@NiFe-MOF/NF) are fabricated, in which the Fe-Ni<sub>3</sub>S<sub>2</sub> clusters could effectively restrain the aggregation of the layer metal-organic frameworks (MOF) nanosheets and adjust the local electronic structures of MOFs nanosheets. Benefiting from the rapid charge transfer and the exposure of abundant active sites, the well-designed Fe-Ni<sub>3</sub>S<sub>2</sub>@NiFe-MOF/NF displays excellent oxygen evolution reaction (OER) and hydrogen evolution reaction (HER) performance. More importantly, when equipped in the alkaline water electrolyzer, the Fe-Ni<sub>3</sub>S<sub>2</sub>@NiFe-MOF/NF enables the system with a mere 1.6 V for achieving the current density of 10 mA cm<sup>-2</sup>. This work offers a paradigm for designing efficient bifunctional HER/OER electrocatalysts based on the hybrid materials of nanostructured metal sulfide and MOF.

**Keywords:** metal-organic frameworks, metal sulfides, nanosheet arrays, electrocatalysts, water splitting

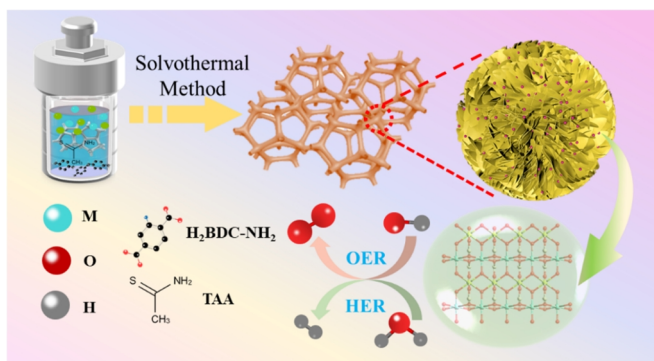


## n TEXT

Electrochemical water splitting is one of the most significant routes to generate the high purity H<sub>2</sub> without harmful side products, which can reconcile the environmental deterioration and excessive consumption of fossil fuels.<sup>[1,2]</sup> Unfortunately, this strategy still suffers from great challenges because the highly scarce and expensive noble metal-based materials are regarded as the best electrocatalysts to decrease the overpotentials and elevate the sluggish dynamic of the two half-reactions: the hydrogen evolution reaction (HER) at cathode and the oxygen evolution reaction (OER) at anode.<sup>[3-6]</sup> Therefore, it is urgent to design and develop inexpensive catalysts extracted from earth-abundant non-noble metal elements as promising alternatives to maximize the water splitting efficiency.<sup>[3-5]</sup> Among various alternative catalysts, metal-organic frameworks (MOF) built from metal ions/clusters and organic linkers are of particular attention as they have the advantages including tailorable pore structure, high surface area and fascinating structural diversity.<sup>[6,7]</sup> For instance, Li et al. synthesized a series of trimetallic Mn<sub>x</sub>Fe<sub>y</sub>Ni-MOF-74 films in-situ grown on nickel foam (NF), which exhibited excellent OER and HER performance in alkaline media.<sup>[8]</sup> Wang et al. reported the NiFe-bimetal two-dimensional ultrathin MOFs nanosheets (NiFe-UMNs) with a uniform thickness of ~10 nm as OER electrocatalysts, delivering excellent catalytic OER activity along with outstanding durability.<sup>[9]</sup> Despite the considerable progress that has been made, the MOF electrocatalysts still suffer from unsatisfactory electrical conductivity and sluggish mass transfer.<sup>[10]</sup>

Recently, MOF has been successfully utilized as a precursor or sacrificial template to fabricate metal derivatives (oxides, hydroxides, phosphides, sulfides, et al.) for improving electrical conductivity and catalytic activity through the pyrolysis strategy.<sup>[11-13]</sup> The high temperature thermal treatments, however, would possibly damage the desirable porous MOF structure, which could result in the aggregation of metal derivatives and deficiency of corresponding active sites, thus decreasing electrocatalytic performance towards water splitting.<sup>[12,14]</sup> To resolve these problems, direct coupling of metal derivatives (e.g. metal oxides, hydroxides, and phosphides) with porous MOF materials is regarded as a brilliant way to not only improve the electrical conductivity but also take full advantage of the unique features of MOF.<sup>[15-17]</sup> The possible coupling between MOF and metal derivatives could induce synergistic effect to facilitate the adsorption/desorption process of reaction intermediates for promoting water-splitting efficiency. However, there is still much room to boost the catalytic activity. It is well known that metal sulfides with plentiful bridged bonds of metal and sulfur possess a high electrical conductivity and great corrosion resistance, providing a big chance to accelerate the charge transfer and improve catalytic activity.<sup>[7,18-20]</sup> To the best of our knowledge, there is rare report on the combination of metal sulfides and MOFs for achieving excellent catalytic performance.

Herein, a facile one-step solvothermal strategy is applied to fabricate an advanced bifunctional HER/OER electrocatalyst via assembling Fe doped Ni<sub>3</sub>S<sub>2</sub> clusters with hierarchical Ni/Fe-based MOF nanosheets array onto Ni foam (denoted as Fe-Ni<sub>3</sub>S<sub>2</sub>@NiFe-MOF/NF). The marriage of clusters and ordered nanosheet arrays



**Scheme 1.** Schematic illustration of the fabrication processes of Fe-Ni<sub>3</sub>S<sub>2</sub>@NiFe-MOF/NF as an effective electrocatalyst for HER/OER.

could not only endow the elaborate Fe-Ni<sub>3</sub>S<sub>2</sub>@NiFe-MOF/NF with large specific surface area, but also facilitate the diffusion of electrolyte ions and the release of produced bubbles, thus boosting the catalytic HER/OER activity compared to the individual catalysts alone. More importantly, the strong electronic interaction between the Fe-Ni<sub>3</sub>S<sub>2</sub> clusters and NiFe-MOF nanosheet arrays could accelerate the charge transfer and optimize the binding strength of the HER/OER intermediates on the catalyst surface. Impressively, the optimized Fe-Ni<sub>3</sub>S<sub>2</sub>@NiFe-MOF/NF not only exhibits excellent catalytic OER activity with a low overpotential of 226 mV at the current density of 100 mA cm<sup>-2</sup>, but also displays outstanding catalytic activity towards HER with the requirement of only 170 mV to drive 50 mA cm<sup>-2</sup>, which are superior to the Fe-Ni<sub>3</sub>S<sub>2</sub>/NF and NiFe-MOF/NF in alkaline electrolyte. In addition, the assembled overall water-splitting system with Fe-Ni<sub>3</sub>S<sub>2</sub>@NiFe-MOF/NF serving as both cathode and anode just requires 1.60 V cell voltage to realize the current density of 10 mA cm<sup>-2</sup>.

As illustrated in Scheme 1, the Fe-Ni<sub>3</sub>S<sub>2</sub>@NiFe-MOF/NF is in-situ grown on 3D macroporous NF substrate via a simple solvothermal strategy. During the solvothermal process, exogenously introduced Ni and Fe ions would coordinate with the 2-aminoterephthalic acid (H<sub>2</sub>BDC-NH<sub>2</sub>) ligand to form NiFe-MOF. Meanwhile, thioacetamide (TAA) as a sulfur source decomposes to release S<sup>2-</sup> ions, which could directly react with the introduced Ni and Fe to form Fe-Ni<sub>3</sub>S<sub>2</sub> on the surface of NiFe-MOF. With the process of reaction, the color of the NF surface completely transforms from silver-gray to brownish black without any speckle, indicating the as-obtained Fe-Ni<sub>3</sub>S<sub>2</sub>@NiFe-MOF/NF is uniformly covered on the NF substrate (Figure S1). For comparison, the pure NiFe-MOF/NF and Fe-Ni<sub>3</sub>S<sub>2</sub>/NF are also synthesized using the same procedure as Fe-Ni<sub>3</sub>S<sub>2</sub>@NiFe-MOF/NF, except for no adding TAA and H<sub>2</sub>BDC-NH<sub>2</sub> linkers, respectively.

The X-ray diffraction (XRD) technique is conducted to investigate the crystal structure of the as-prepared Fe-Ni<sub>3</sub>S<sub>2</sub>/NF, NiFe-MOF/NF, and Fe-Ni<sub>3</sub>S<sub>2</sub>@NiFe-MOF/NF. As shown in Figure 1a, it is evident that all three samples in XRD pattern display similarly prominent diffraction peaks at 44.5, 51.8, and 76.4°, corresponding to the NF substrate (JCPDS No. 65-2865).<sup>[21]</sup> The pure Fe-Ni<sub>3</sub>S<sub>2</sub>/NF exhibits the characteristic diffraction peaks at 21.9, 31.3, 38.0, 50.1, and 55.4°, which can be indexed to the (101), (110), (003), (113) and (122) of Ni<sub>3</sub>S<sub>2</sub> hexagonal planes.<sup>[17,22,23]</sup> It can be

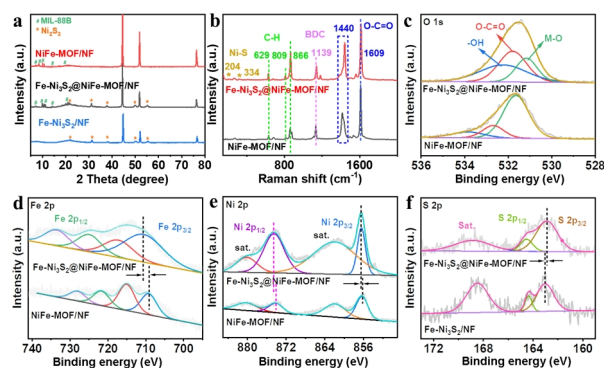


**Figure 1.** (a) XRD patterns of Fe-Ni<sub>3</sub>S<sub>2</sub>@NiFe-MOF/NF, NiFe-MOF/NF and Fe-Ni<sub>3</sub>S<sub>2</sub>/NF. (b) Raman spectra of Fe-Ni<sub>3</sub>S<sub>2</sub>@NiFe-MOF/NF and NiFe-MOF/NF. High-resolution XPS spectra of (c) C 1s, (d) Fe 2p, (e) Ni 2p, and (f) S 2p for the electrocatalysts.

seen that the diffraction peaks of Fe-Ni<sub>3</sub>S<sub>2</sub>/NF slightly shift to the high-angle direction compared to those of the Ni<sub>3</sub>S<sub>2</sub> hexagonal structure previously reported,<sup>[23]</sup> indicating the possible doping of Fe into Ni<sub>3</sub>S<sub>2</sub> framework. For pure NiFe-MOF/NF, the characteristic peaks recorded at 9.2, 10.5, 12.5, 16.7, and 20.7° agree well with what have previously reported for MIL-88B type MOF structure.<sup>[24]</sup> As observed, all the above mentioned diffraction peaks of NiFe-MOF/NF and Fe-Ni<sub>3</sub>S<sub>2</sub>/NF could be clearly detected in the XRD pattern of Fe-Ni<sub>3</sub>S<sub>2</sub>@NiFe-MOF/NF, demonstrating the successful formation of NiFe-MOF and Fe-Ni<sub>3</sub>S<sub>2</sub> in as-fabricated Fe-Ni<sub>3</sub>S<sub>2</sub>@NiFe-MOF/NF. The Raman spectra are recorded to reveal functional groups of the as-prepared Fe-Ni<sub>3</sub>S<sub>2</sub>/NF, NiFe-MOF/NF, and Fe-Ni<sub>3</sub>S<sub>2</sub>@NiFe-MOF/NF. As shown in Figure S2, the appearance of peaks at ~194, 344 and 677 cm<sup>-1</sup> clearly validate the formation of Ni-S species for pure Fe-Ni<sub>3</sub>S<sub>2</sub>/NF.<sup>[23]</sup> A shoulder peak at 310 cm<sup>-1</sup> can also be observed, which is assigned to the Fe-S species.<sup>[23]</sup> The characteristic peaks associated with the vibration mode of the H<sub>2</sub>BDC-NH<sub>2</sub> linkers are observed in the spectra of pure NiFe-MOF/NF (Figure 1b). The peaks at ~629, 809, and 866 cm<sup>-1</sup> are related to the stretching mode of C-H from benzene ring,<sup>[25,26]</sup> while a new doublet at ~1440 and 1609 cm<sup>-1</sup> is matched well with the in- and out-of-phase stretching modes of the carboxylate group, indicating the successful coordination between Ni/Fe ions and H<sub>2</sub>BDC-NH<sub>2</sub> linkers in NiFe-MOF/NF.<sup>[25,27]</sup> It is worth noting that the Fe-Ni<sub>3</sub>S<sub>2</sub>@NiFe-MOF/NF possesses all the Raman signals nearly identical to those of NiFe-MOF/NF and Fe-Ni<sub>3</sub>S<sub>2</sub>/NF, verifying the coexistence of Fe-Ni<sub>3</sub>S<sub>2</sub> and NiFe-MOF, which agree well with the XRD results.

The chemical components and valence state of the as-prepared Fe-Ni<sub>3</sub>S<sub>2</sub>@NiFe-MOF/NF are probed through X-ray photoelectron spectroscopy (XPS). As shown in Figure S3, the whole XPS survey spectrum demonstrates the presence of Ni, Fe, S and O elements on the surface of Fe-Ni<sub>3</sub>S<sub>2</sub>@NiFe-MOF/NF. As shown in O 1s spectrum of Fe-Ni<sub>3</sub>S<sub>2</sub>@NiFe-MOF/NF (Figure 1c), the characteristic peak at 533.7 eV could be attributed to the -OH group originated from the adsorbed H<sub>2</sub>O molecules, while the peaks at 531.6 and 532.7 eV are ascribed to the O-C=O and M-O bonds, respectively.<sup>[28,29]</sup> Figure 1d presents that the Fe 2p spectrum of Fe-Ni<sub>3</sub>S<sub>2</sub>@NiFe-MOF/NF could be divided into a pair

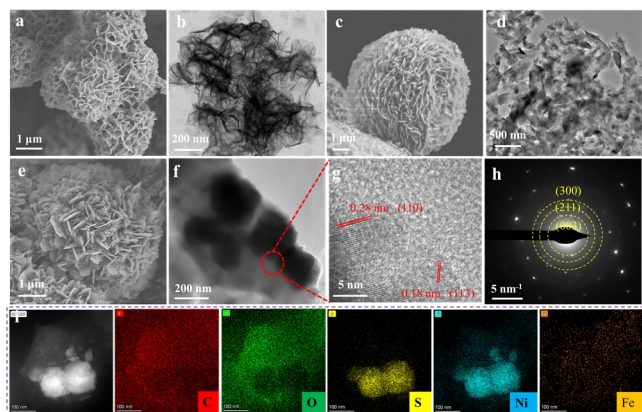


**Figure 2.** (a) SEM images and (b) TEM images of Fe-Ni<sub>3</sub>S<sub>2</sub>/NF. (c) SEM images and (d) TEM images of NiFe-MOF/NF. (e) SEM images, (f) TEM images, (g) HR-TEM images, (h) SAED pattern, (i) HAADF-STEM image and corresponding elemental mapping images of Fe-Ni<sub>3</sub>S<sub>2</sub>@NiFe-MOF/NF.

of peaks at 711.1 and 725.1 eV assigned to Fe 2p<sub>3/2</sub> and Fe 2p<sub>1/2</sub>, indicating the existence of Fe<sup>3+</sup>. The characteristic peaks at 856.3 and 874.6 eV for the Ni 2p spectrum can be indexed to the Ni 2p<sub>3/2</sub> and Ni 2p<sub>1/2</sub> (Figure 2e), confirming the +2 oxidation state of Ni in Fe-Ni<sub>3</sub>S<sub>2</sub>@NiFe-MOF/NF.<sup>[22,29,30]</sup> In the S 2p spectrum of Fe-Ni<sub>3</sub>S<sub>2</sub>@NiFe-MOF/NF (Figure 2f), the two characteristic peaks centered at 162.9 and 164.6 eV are representative of the S 2p<sub>3/2</sub> and S 2p<sub>1/2</sub>, respectively.<sup>[30]</sup> Compared to NiFe-MOF/NF, the Ni 2p and Fe 2p peaks are positively shifted by ~0.4 and 1.2 eV for the Fe-Ni<sub>3</sub>S<sub>2</sub>@NiFe-MOF/NF, respectively. The positive shift of Fe 2p peaks is mainly attributed to the formation of Fe-S bridging units,<sup>[10]</sup> which is consistent with the above XRD and Raman results. The S 2p peaks can be observed to be negatively shifted by ~0.3 eV compared to that of the Fe-Ni<sub>3</sub>S<sub>2</sub>/NF, suggesting the probable existence of electron coupling interaction between NiFe-MOF and Fe-Ni<sub>3</sub>S<sub>2</sub>, which is conducive to promoting the charge transfer and reaction kinetics of Fe-Ni<sub>3</sub>S<sub>2</sub>@NiFe-MOF/NF.<sup>[17]</sup>

The morphology structures of as-prepared Fe-Ni<sub>3</sub>S<sub>2</sub>/NF, NiFe-MOF/NF, and Fe-Ni<sub>3</sub>S<sub>2</sub>@NiFe-MOF/NF are characterized by field-emission scanning electron microscopy (FE-SEM) and transmission electron microscopy (TEM). For pure Fe-Ni<sub>3</sub>S<sub>2</sub>/NF, the 3D honeycomb-like morphology composed of densely interlaced nanosheets can be observed in Figure 2a and 2b. The pure NiFe-MOF/NF displays aggregated nanosheet array structure (Figure 2c and 2d), while the as-fabricated Fe-Ni<sub>3</sub>S<sub>2</sub>@NiFe-MOF/NF shows the coupled well-dispersed nanosheet arrays with the Fe-Ni<sub>3</sub>S<sub>2</sub> nanoclusters. Such nanoclusters could effectively weaken the interaction between MOF nanosheets, e.g. van der Waals forces and p-p stacking, preventing the aggregation of NiFe-MOF nanosheets. TEM images of Fe-Ni<sub>3</sub>S<sub>2</sub>@NiFe-MOF/NF further unveil that the nanoclusters with the size of 100-200 nm are coated on the surface of 2D nanosheet (Figure 2f). High-resolution TEM (HR-TEM) is performed to further obtain the information of local morphology and microstructure of Fe-Ni<sub>3</sub>S<sub>2</sub>@NiFe-MOF/NF. As shown in Figure 2g, the Fe-Ni<sub>3</sub>S<sub>2</sub>@NiFe-MOF/NF possesses a well-defined phase interface on the surface, in which the visible

lattice fringes separated by the interplanar spacing of 0.28 and 0.18 nm can be coincided with the d-spacing of the (110) and (113) crystalline planes of the Fe-Ni<sub>3</sub>S<sub>2</sub>, respectively.<sup>[17,22,30]</sup> Some bright diffraction spots could be clearly observed in the selected area electron diffraction (SAED) pattern (Figure 2h), which correspond to the (003), (211), and (300) planes of Fe-Ni<sub>3</sub>S<sub>2</sub>, respectively.<sup>[22]</sup> It is not visible for the lattice fringes and diffraction pattern that are indexed to the MIL-88B, which may be caused by the damage of NiFe-MOF structure under the high-energy electron flow.<sup>[31]</sup> The elemental mapping is conducted to analyze the distribution of different elements in Fe-Ni<sub>3</sub>S<sub>2</sub>@NiFe-MOF/NF. It can be seen in Figure 2i that the Ni, Fe, O, and C are uniformly distributed over the entire Fe-Ni<sub>3</sub>S<sub>2</sub>@NiFe-MOF/NF. As observed, the elemental mapping of the collected S and Ni is strong in the clusters portion of Fe-Ni<sub>3</sub>S<sub>2</sub>@NiFe-MOF/NF, which indicates the formation of Fe-Ni<sub>3</sub>S<sub>2</sub> clusters on the NiFe-MOF surface. Such unique structure is expected to accelerate the electron/mass transfer, electrolyte permeation as well as the release of generated gases, which can be effective to promote the catalytic activity.

The electrochemical OER performances of the resultant Fe-Ni<sub>3</sub>S<sub>2</sub>@NiFe-MOF/NF, together with NiFe-MOF/NF, Fe-Ni<sub>3</sub>S<sub>2</sub>/NF, RuO<sub>2</sub> and blank NF for comparison, are evaluated in 1.0 M KOH solution using a standard three-electrode cell configuration. As shown in Figure 3a, the blank NF exhibits negligible anodic currents before 1.65 V vs. RHE. For Fe-Ni<sub>3</sub>S<sub>2</sub>@NiFe-MOF/NF, NiFe-MOF/NF, and Fe-Ni<sub>3</sub>S<sub>2</sub>/NF, the appearance of the peaks located at ca. 1.37 V vs. RHE implies the surface oxidation of the partial Ni<sup>2+</sup> to form Ni<sup>3+</sup>.<sup>[6,32]</sup> The overpotential to deliver the current density of 100 mA cm<sup>-2</sup> is as low as 226 mV for Fe-Ni<sub>3</sub>S<sub>2</sub>@NiFe-MOF/NF, which is much smaller than those of NiFe-MOF/NF (292 mV), Fe-Ni<sub>3</sub>S<sub>2</sub>/NF (272 mV) and commercial RuO<sub>2</sub> (362 mV). The corresponding Tafel slope is applied to evaluate the catalytic OER

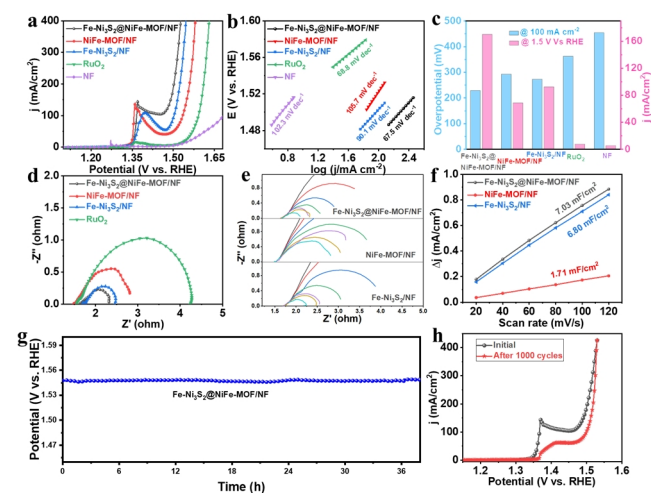


**Figure 3.** (a) LSV curves at a scan rate of 5 mV s<sup>-1</sup>, (b) the corresponding Tafel plots, (c) the current density at 1.50 V versus RHE and the overpotential at 10 mA cm<sup>-2</sup> for the Fe-Ni<sub>3</sub>S<sub>2</sub>/NF, NiFe-MOF/NF, Fe-Ni<sub>3</sub>S<sub>2</sub>@NiFe-MOF/NF, RuO<sub>2</sub>, and the blank NF. (d) EIS spectra, (e) Nyquist plots at various potentials, and (f) the C<sub>d</sub> values for the as-prepared Fe-Ni<sub>3</sub>S<sub>2</sub>/NF, NiFe-MOF/NF, and Fe-Ni<sub>3</sub>S<sub>2</sub>@NiFe-MOF/NF. (g) Chronopotentiometry curve at 50 mA cm<sup>-2</sup>, and (h) LSV curves before and after 1000 CV cycles for the Fe-Ni<sub>3</sub>S<sub>2</sub>@NiFe-MOF/NF.

kinetics.<sup>[33]</sup> As shown in Figure 3b, the calculated Tafel slope value of Fe-Ni<sub>3</sub>S<sub>2</sub>@NiFe-MOF/NF (67.5 mV dec<sup>-1</sup>) is lower than those of NiFe-MOF/NF (105.7 mV dec<sup>-1</sup>), Fe-Ni<sub>3</sub>S<sub>2</sub>/NF (90.1 mV dec<sup>-1</sup>) and commercial RuO<sub>2</sub> (68.8 mV dec<sup>-1</sup>), manifesting its remarkable OER dynamic behavior. As expected, when the potential is fixed at 1.50 V vs. RHE, the Fe-Ni<sub>3</sub>S<sub>2</sub>@NiFe-MOF/NF can get a high current density of 170 mA cm<sup>-2</sup> (Figure 3c), 3-fold, 2-fold, 23-fold, and 33-fold higher than NiFe-MOF/NF (60.5 mA cm<sup>-2</sup>), Fe-Ni<sub>3</sub>S<sub>2</sub>/NF (92.3 mA cm<sup>-2</sup>), RuO<sub>2</sub>/NF (7.3 mA cm<sup>-2</sup>) and blank Ni foam (5.2 mA cm<sup>-2</sup>), respectively. Electrochemical impedance spectroscopy (EIS) is carried out to assess the charge transfer resistance (R<sub>ct</sub>) at the electrode/electrolyte interface.<sup>[34]</sup> As presented in Figure 3d, Nyquist plots reveal that Fe-Ni<sub>3</sub>S<sub>2</sub>@NiFe-MOF/NF has the smallest semicircle among all the investigated samples, indicating its lowest R<sub>ct</sub>.<sup>[34]</sup> With increasing the potential gradually, the semicircle diameter reduced the most rapidly in Fe-Ni<sub>3</sub>S<sub>2</sub>@NiFe-MOF/NF compared with other counterparts (Figure 3e), indicating the Fe-Ni<sub>3</sub>S<sub>2</sub>@NiFe-MOF/NF is easier to be polarized during OER process,<sup>[35]</sup> which could facilitate the charge transfer linked to the adsorption/desorption of OER reaction intermediates. The electrochemical active surface area (ECSA) is also investigated to evaluate the OER activities by calculating the double-layer capacitance (C<sub>dl</sub>), which is obtained via recording the cyclic voltammetry (CV) curves at different scan rates in a non-faradic potential range. The C<sub>dl</sub> value of Fe-Ni<sub>3</sub>S<sub>2</sub>@NiFe-MOF/NF is calculated to be 7.03 mF cm<sup>-2</sup> (Figure 3f), higher than that of NiFe-MOF/NF (6.80 mF cm<sup>-2</sup>) and Fe-Ni<sub>3</sub>S<sub>2</sub>/NF (1.71 mF cm<sup>-2</sup>), suggesting that Fe-Ni<sub>3</sub>S<sub>2</sub>@NiFe-MOF/NF with unique arrays structure could provide more accessible active sites to boost the catalytic OER activity. The LSV curves normalized by ECSA display that the Fe-Ni<sub>3</sub>S<sub>2</sub>@NiFe-MOF/NF affords higher specific activity than other counterparts (Figure S4), further disclosing the marriage of Fe-Ni<sub>3</sub>S<sub>2</sub> clusters and NiFe-MOF nanosheet arrays endows the catalysts with high specific activity.

Apart from the catalytic activity, the prolonged durability is considered as another important parameter to assess the OER performance.<sup>[36]</sup> The 1000 cycles are handled for Fe-Ni<sub>3</sub>S<sub>2</sub>@NiFe-MOF/NF using a successive CV scanning between 1.2 and 1.5 V vs. RHE. As displayed in Figure 3g, the negligible potential loss can be observed from the polarization curve of Fe-Ni<sub>3</sub>S<sub>2</sub>@NiFe-MOF/NF after 1000 CV cycles compared with the initial one, especially at the high potential region, which suggests that the Fe-Ni<sub>3</sub>S<sub>2</sub>@NiFe-MOF/NF possesses the exceptional cycling durability during the OER process. In addition, the chronopotentiometric (v-t) measurement is carried out to further evaluate the long-term stability of Fe-Ni<sub>3</sub>S<sub>2</sub>@NiFe-MOF/NF. It should be noted that the studied Fe-Ni<sub>3</sub>S<sub>2</sub>@NiFe-MOF/NF exhibits negligible decay of potential after a 36h continuous test with a permanent current density of 50 mA cm<sup>-2</sup> (Figure 3h), further demonstrating the outstanding OER stability. The significantly enhanced OER performance could be ascribed to the hierarchical array structure and the synergistic effect between NiFe-MOF and Fe-Ni<sub>3</sub>S<sub>2</sub>, which is conducive to facilitating the charge/mass transfer and the adsorption/desorption of OER reaction intermediates.

The XRD is employed to investigate the structure evolution of Fe-Ni<sub>3</sub>S<sub>2</sub>@NiFe-MOF/NF after the OER test. As shown in Figure

S5, the characteristic peaks of NiFe-MOF completely disappear, while the peaks of Fe-Ni<sub>3</sub>S<sub>2</sub> have no obvious change. The results suggest that the NiFe-MOF may undergo structural change from crystalline MOF to amorphous hydroxide,<sup>[37,38]</sup> whereas the structure of Fe-Ni<sub>3</sub>S<sub>2</sub> can be well kept during the OER process. The disordered hydroxide generated from the conversion of NiFe-MOF may prevent the Fe-Ni<sub>3</sub>S<sub>2</sub> clusters from being reconstructed. The SEM images show that the morphology of Fe-Ni<sub>3</sub>S<sub>2</sub>@NiFe-MOF/NF still maintains the array structure after the OER test, whereas the nanosheets become wrinkled and the thickness obviously increases (Figure S6), suggesting the possible generation of hydroxides during OER process. The XPS technique is applied to further investigate the structural change of Fe-Ni<sub>3</sub>S<sub>2</sub>@NiFe-MOF/NF during the OER process, as shown in Figure S7. In the O 1s spectrum, the percentage of M-O bond obviously increases and that of O-C=O bond decreases after OER durability test, further suggesting the conversion of NiFe-MOF to hydroxides during OER process.<sup>[11,17,22]</sup> Notably, the binding energy of Ni 2p and Fe 2p peaks present the obviously positive shift for Fe-Ni<sub>3</sub>S<sub>2</sub>@NiFe-MOF/NF after the OER test, revealing that the metal species in Fe-Ni<sub>3</sub>S<sub>2</sub>@NiFe-MOF/NF could be converted to be electron-rich state during OER process, which is convenient to the formation of hydroxide.<sup>[37]</sup> Therefore, it could be concluded that the formed hydroxide may serve as the real active sites in the OER process.

Besides the promising applications for OER, the HER activity of Fe-Ni<sub>3</sub>S<sub>2</sub>@NiFe-MOF/NF is also investigated in 1M KOH solution. It is found that the HER activity of Fe-Ni<sub>3</sub>S<sub>2</sub>@NiFe-MOF/NF is better than that of NiFe-MOF/NF and Fe-Ni<sub>3</sub>S<sub>2</sub>/NF, although it is inferior to that of commercial Pt/C (Figure 4a and 4b). The needed

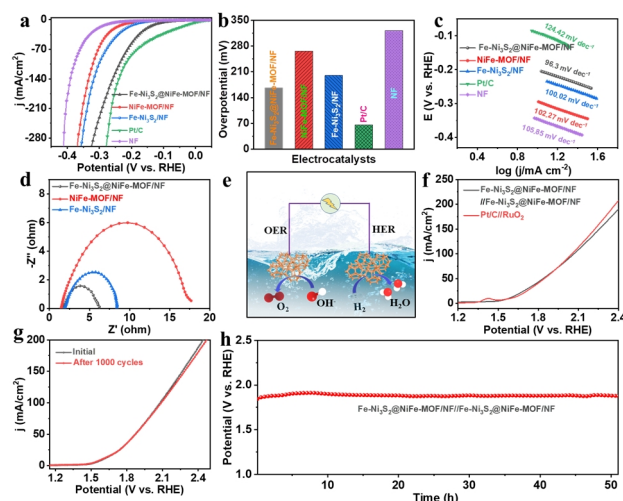


**Figure 4.** (a) LSV curves, (b) the corresponding overpotentials at current density of 50 mA cm<sup>-2</sup>, and (c) Tafel plots of Fe-Ni<sub>3</sub>S<sub>2</sub>/NF, NiFe-MOF/NF, Fe-Ni<sub>3</sub>S<sub>2</sub>@NiFe-MOF/NF, Pt/C, and the blank NF. (d) Nyquist plots of the as-fabricated Fe-Ni<sub>3</sub>S<sub>2</sub>/NF, NiFe-MOF/NF, and Fe-Ni<sub>3</sub>S<sub>2</sub>@NiFe-MOF/NF. (e) Schematic illustration of the electrolyzer using Fe-Ni<sub>3</sub>S<sub>2</sub>@NiFe-MOF/NF as both anode and cathode. (f) LSV curves for the couple of Fe-Ni<sub>3</sub>S<sub>2</sub>@NiFe-MOF/NF//Fe-Ni<sub>3</sub>S<sub>2</sub>@NiFe-MOF/NF and RuO<sub>2</sub>/Pt/C for water electrolysis (without iR compensation). (g) LSV curves before and after 1000 cycles and (h) chronopotentiometric curve at 10 mA cm<sup>-2</sup> for the integrated system.

HER overpotential of Fe-Ni<sub>3</sub>S<sub>2</sub>@NiFe-MOF/NF (170 mV) is lower than those of NiFe-MOF/NF (274 mV) and Fe-Ni<sub>3</sub>S<sub>2</sub>/NF (200 mV) to deliver the current density of 50 mA cm<sup>-2</sup>. The Tafel slope of Fe-Ni<sub>3</sub>S<sub>2</sub>@NiFe-MOF/NF is 96.3 mV dec<sup>-1</sup>, smaller than those of pure NiFe-MOF/NF (102.3 mV dec<sup>-1</sup>) and Fe-Ni<sub>3</sub>S<sub>2</sub>/NF (100.1 mV dec<sup>-1</sup>), demonstrating the fastest HER kinetics (Figure 4c). Such Tafel slope value suggests that the HER pathway of Fe-Ni<sub>3</sub>S<sub>2</sub>@NiFe-MOF/NF corresponds to the Volmer-Heyrovsky mechanism and the desorption of hydrogen is the key rate-determining step.<sup>[39]</sup> As can be seen in Figure 4d, the Fe-Ni<sub>3</sub>S<sub>2</sub>@NiFe-MOF/NF displays the smallest semicircle in the Nyquist plots compared with other counterparts, indicating that the Fe-Ni<sub>3</sub>S<sub>2</sub>@NiFe-MOF/NF has the fastest electron transfer at the electrode/electrolyte interface. After HER process, the diffraction peaks of NiFe-MOF completely disappear while those of Fe-Ni<sub>3</sub>S<sub>2</sub> survive, as shown in the XRD pattern in Figure S8. This may be because the metal sites of NiFe-MOF could be partially reduced and the OH<sup>-</sup> could replace the organic ligands of NiFe-MOF during HER process, leading to the structural transformation from NiFe-MOF to metal hydroxide.<sup>[8,40]</sup> Therefore, the main HER active sites may be the metal hydroxide formed at the Fe-Ni<sub>3</sub>S<sub>2</sub>@NiFe-MOF/NF surface.

Inspired by the outstanding performances of OER and HER, an overall alkaline electrolysis cell is further established by taking Fe-Ni<sub>3</sub>S<sub>2</sub>@NiFe-MOF/NF as both anode and cathode (Figure 4e). As revealed in Figure 4f, the assembled Fe-Ni<sub>3</sub>S<sub>2</sub>@NiFe-MOF/NF//Fe-Ni<sub>3</sub>S<sub>2</sub>@NiFe-MOF/NF system could readily drive water electrolysis with a low cell voltage of 1.60 V to realize the current density of 10 mA cm<sup>-2</sup>, which is comparable to the state-of-the-art coupled RuO<sub>2</sub>/Pt/C under the corresponding current density. After continuous electrolysis for 1 h with an H-type electrolytic cell, the calculated Faraday efficiency is close to 100% by measuring the volume of generated O<sub>2</sub> and H<sub>2</sub> with water drainage method, as shown in Figure S9. The long-term stability of integrated system could be deemed as one of the central interests for practical applications.<sup>[35]</sup> We perform a successive CV scanning between 1.2–1.7 V vs. RHE to investigate the stability for the assembled Fe-Ni<sub>3</sub>S<sub>2</sub>@NiFe-MOF/NF//Fe-Ni<sub>3</sub>S<sub>2</sub>@NiFe-MOF/NF system. The obtained polarization curve after 1000 CV cycles exhibits just a little bit shift compared with the initial one, indicating the excellent stability of the assembled system in 1 M KOH solution (Figure 4g). In addition, a chronopotentiometric test is used to evaluate long-term durability at a constant current density of 50 mA cm<sup>-2</sup> (Figure 4h). As observed, the potential of Fe-Ni<sub>3</sub>S<sub>2</sub>@NiFe-MOF/NF//Fe-Ni<sub>3</sub>S<sub>2</sub>@NiFe-MOF/NF system exhibits only 5% increase at the current density of 50 mA cm<sup>-2</sup> over a period of 50 h, which hence makes the Fe-Ni<sub>3</sub>S<sub>2</sub>@NiFe-MOF/NF a great promising candidate for efficient and durable H<sub>2</sub> generation by water splitting.

## CONCLUSION

In summary, we have successfully designed hierarchical NiFe-MOF nanosheet arrays coupled with Fe-Ni<sub>3</sub>S<sub>2</sub> clusters on the surface of Ni foam substrate via a facile one-step solvothermal reaction. The hierarchical array structure and the synergistic effect between NiFe-MOF and attractive Fe-Ni<sub>3</sub>S<sub>2</sub> could endow the Fe-Ni<sub>3</sub>S<sub>2</sub>@NiFe-MOF/NF with abundant active sites, rapid mass/charge transport, and strong bubble-releasing ability during the

electrochemical reaction process. Remarkably, the Fe-Ni<sub>3</sub>S<sub>2</sub>@NiFe-MOF/NF exhibits excellent catalytic activity and stability towards both OER ( $\eta = 226$  mV at 100 mA cm<sup>-2</sup>) and HER ( $\eta = 170$  mV at 50 mA cm<sup>-2</sup>). More significantly, the assembled Fe-Ni<sub>3</sub>S<sub>2</sub>@NiFe-MOF/NF//Fe-Ni<sub>3</sub>S<sub>2</sub>@NiFe-MOF/NF system could readily drive the current density of 10 mA cm<sup>-2</sup> only at a low cell voltage of 1.60 V. The work provides useful guidelines for the preparation of high-performance bifunctional electrocatalysts and sheds light on the way for rationally designing the hybrid materials based on the MOF and metal sulfide.

## EXPERIMENTAL

**Materials and Reagents.** Ni(NO<sub>3</sub>)<sub>2</sub>·6H<sub>2</sub>O, FeCl<sub>3</sub>·6H<sub>2</sub>O, 2-aminoterephthalic acid (H<sub>2</sub>BDC-NH<sub>2</sub>), and thioacetamide (TAA) were purchased from Aladdin Co., Ltd. (Shanghai, China). Potassium hydroxide, N,N-dimethylformamide (DMF), isopropanol, and ethanol were bought from Sinopharm Chemical Reagent Co. The commercial Pt/C catalyst (20 wt%) and RuO<sub>2</sub> powder (99.9%) were obtained from Johnson Matthey Company (Shanghai, China). Nafion solution (5%) was provided by Sigma-Aldrich (MO, USA). All chemicals and reagents were used directly without further purification.

**Synthesis of Fe-Ni<sub>3</sub>S<sub>2</sub>@NiFe-MOF/NF.** The Fe-Ni<sub>3</sub>S<sub>2</sub>@NiFe-MOF was in situ grown on Ni foam (NF) through a solvothermal method, as illustrated in Scheme 1. Prior to the solvothermal reaction, the commercial NF was ultrasonically treated for 15 min in sequence in 5 M HCl solution, ethanol, and deionized water to clean the surface oxide layers and impurities, followed by drying in vacuum at 50 °C. In the preparation of Fe-Ni<sub>3</sub>S<sub>2</sub>@NiFe-MOF/NF, a homogeneous mixture containing 54 mg FeCl<sub>3</sub>·6H<sub>2</sub>O, 291 mg Ni(NO<sub>3</sub>)<sub>2</sub>·6H<sub>2</sub>O, 181 mg 2-aminoterephthalic acid (H<sub>2</sub>BDC-NH<sub>2</sub>), 75 mg TAA, 30 mL DMF and 8 mL ethanol was poured into the Teflon-lined stainless-steel autoclave and the pretreated Ni foam was immersed in the above solution. Then, the autoclave was sealed for reaction at 150 °C for 15 h. After cooling down to room temperature, the resulting NF was taken out and thoroughly rinsed with ethanol and deionized water for three times before drying at 50 °C in vacuum. The loading amount of the Fe-Ni<sub>3</sub>S<sub>2</sub>@NiFe-MOF on the NF was around 1.2 mg cm<sup>-2</sup>.

**Synthesis of NiFe-MOF/NF.** The same procedures described above were applied for the preparation of NiFe-MOF/NF except for no TAA involved in the mixed solution.

**Synthesis of Fe-Ni<sub>3</sub>S<sub>2</sub>/NF.** The same procedures described above were applied for the preparation of Fe-Ni<sub>3</sub>S<sub>2</sub>/NF except that no H<sub>2</sub>BDC-NH<sub>2</sub> ligands were added into the solution.

**Preparation of Pt/C and RuO<sub>2</sub>.** 5 mg Pt/C (20 wt%) or RuO<sub>2</sub> powder (99.9%) was dispersed in the mixture solution of deionized water/isopropanol/5% Nafion (v:v:v = 4:1:0.1). After ultrasonication for 1 h, the as-prepared catalyst ink was uniformly loaded on the surface of NF and dried under infrared light. The mass loading of the Pt/C or RuO<sub>2</sub> catalyst powder on Ni film was ~1.2 mg cm<sup>-2</sup>.

**Material Characterizations.** The powder X-ray diffraction (XRD) patterns were recorded on a Bruker D8 Advanced Diffractometer

(Cu K $\alpha$  radiation,  $\lambda = 1.5418 \text{ \AA}$ ). Raman measurements were carried out on the Thermo Fisher spectrometer equipped by using a 532 nm laser as the excitation source. The surface morphology, composition and microstructure of the as-prepared samples were characterized via scanning electron microscopy (SEM, Hitachi S-4800) and transmission electron microscopy (TEM, JEOL JEM 2100). X-ray photoelectron spectroscopy (XPS) measurements were carried out on the Thermo Scientific ESCALAB 250Xi spectrometer.

**Electrochemical Measurements.** The electrocatalytic activities towards HER and OER were tested by the electrochemical workstation (CHI 760E, Shanghai) with a three-electrode system or two-electrode electrochemical cell. The OER and HER performances were investigated in 1.0 M KOH using the NF-based electrodes as the working electrode, the graphite rod and Hg/HgO electrode as counter and reference electrodes, respectively. All potentials for OER and HER in this work were converted to the reversible hydrogen electrode (RHE) potential according to the Nernst equation:  $E_{\text{RHE}} = E_{\text{Hg/HgO}} + 0.059\text{pH} + 0.197$ . The performances of overall water splitting were measured with a two-electrode configuration cell, in which the Fe-Ni<sub>3</sub>S<sub>2</sub>@NiFe-MOF/NF was applied as both anode and cathode. The linear sweep voltammetry (LSV) curves were collected at a scan rate of 5 mV s<sup>-1</sup> with automatic iR compensation on the electrochemical workstation. To evaluate the electrochemical active surface area (ECSA), the electrochemical double layer capacitances ( $C_{\text{dl}}$ ) were obtained by recording the CV curves in a non-Faradaic potential region from 0.401 to 0.501 V vs. RHE at different scan rates of 20, 40, 60, 80, 100, and 120 mV s<sup>-1</sup>.

## n ACKNOWLEDGEMENTS

This work was financially supported by the Natural Science Foundation of Shandong Province (ZR2020ZD10), and the National Natural Science Foundation of China (21775142).

## n AUTHOR INFORMATION

Corresponding authors. Emails: chulei@ouc.edu.cn and huangminghua@ouc.edu.cn

## n AUTHOR CONTRIBUTION

# These authors contributed equally to this work.

## n COMPETING INTERESTS

The authors declare no competing interests.

## n ADDITIONAL INFORMATION

Supplementary information is available for this paper at <http://manu30.magtech.com.cn/jghx/EN/10.14102/j.cnki.0254-5861.2022-0145>

For submission: <https://mc03.manuscriptcentral.com/cjsc>

## n REFERENCES

(1) Li, H.; Di, S.; Niu, P.; Wang, S.; Wang, J.; Li, L. A durable half-metallic diatomic catalyst for efficient oxygen reduction. *Energy Environ. Sci.* **2022**, 15, 1601-1610.

(2) Wang, H.; Liu, X.; Niu, P.; Wang, S.; Shi, J.; Li, L. Porous two-dimensional materials for photocatalytic and electrocatalytic applications. *Matter* **2020**, 2, 1377-1413.

(3) Wu, Y.; Wang, H.; Ji, S.; Pollet, B. G.; Wang, X.; Wang, R. Engineered porous Ni<sub>2</sub>P-nanoparticle/Ni<sub>2</sub>P-nanosheet arrays via the Kirkendall effect and Ostwald ripening towards efficient overall water splitting. *Nano Res.* **2020**, 13, 2098-2105.

(4) Ding, W.-L.; Cao, Y.-H.; Liu, H.; Wang, A.-X.; Zhang, C.-J.; Zheng, X.-R. In situ growth of NiSe@Co<sub>0.85</sub>Se heterointerface structure with electronic modulation on nickel foam for overall water splitting. *Rare Met.* **2020**, 40, 1373-1382.

(5) Wang, C.-Y.; Yang, C.-H.; Zhang, Z.-C. Unraveling molecular-level mechanisms of reactive facet of carbon nitride single crystals photocatalyzing overall water splitting. *Rare Met.* **2020**, 39, 1353-1355.

(6) Zhou, J.; Han, Z.; Wang, X.; Gai, H.; Chen, Z.; Guo, T.; Hou, X.; Xu, L.; Hu, X.; Huang, M.; Levchenko, S. V.; Jiang, H. Discovery of quantitative electronic structure-OER activity relationship in metal-organic framework electrocatalysts using an integrated theoretical-experimental approach. *Adv. Funct. Mater.* **2021**, 31, 2102066.

(7) He, P.; Xie, Y.; Dou, Y.; Zhou, J.; Zhou, A.; Wei, X.; Li, J. R. Partial sulfurization of a 2D MOF array for highly efficient oxygen evolution reaction. *ACS Appl. Mater. Interfaces* **2019**, 11, 41595-41601.

(8) Zhou, W.; Xue, Z.; Liu, Q.; Li, Y.; Hu, J.; Li, G. Trimetallic MOF-74 films grown on Ni foam as bifunctional electrocatalysts for overall water splitting. *ChemSusChem* **2020**, 13, 5647-5653.

(9) Hai, G.; Jia, X.; Zhang, K.; Liu, X.; Wu, Z.; Wang, G. High-performance oxygen evolution catalyst using two-dimensional ultrathin metal-organic frameworks nanosheets. *Nano Energy* **2018**, 44, 345-352.

(10) Ma, X.; Chang, C.; Zhang, Y.; Niu, P.; Liu, X.; Wang, S.; Li, L. Synthesis of Co-based Prussian blue analogues/dual-doped hollow carbon microsphere hybrids as high-performance bifunctional electrocatalysts for oxygen evolution and overall water splitting. *ACS Sustain. Chem. Eng.* **2020**, 8, 8318-8326.

(11) Sun, H.; Lian, Y.; Yang, C.; Xiong, L.; Qi, P.; Mu, Q.; Zhao, X.; Guo, J.; Deng, Z.; Peng, Y. A hierarchical nickel-carbon structure templated by metal-organic frameworks for efficient overall water splitting. *Energy & Environ. Sci.* **2018**, 11, 2363-2371.

(12) Jiao, L.; Wang, Y.; Jiang, H. L.; Xu, Q. Metal-organic frameworks as platforms for catalytic applications. *Adv. Mater.* **2018**, 30, e1703663.

(13) Lyu, F.; Bai, Y.; Li, Z.; Xu, W.; Wang, Q.; Mao, J.; Wang, L.; Zhang, X.; Yin, Y. Self-templated fabrication of CoO-MoO<sub>2</sub> nanocages for enhanced oxygen evolution. *Adv. Funct. Mater.* **2017**, 27, 1702324.

(14) Duan, J.; Chen, S.; Zhao, C. Ultrathin metal-organic framework array for efficient electrocatalytic water splitting. *Nat. Commun.* **2017**, 8, 15341.

(15) Wang, W.; Wang, Z.; Hu, Y.; Liu, Y.; Chen, S. A potential-driven switch of activity promotion mode for the oxygen evolution reaction at Co<sub>3</sub>O<sub>4</sub>/NiO<sub>x</sub>H<sub>y</sub> interface. *eScience* **2022**, <https://doi.org/10.1016/j.esci.2022.04.004>.

(16) Cho, K.; Han, S. H.; Suh, M. P. Copper-organic framework fabricated with CuS nanoparticles: synthesis, electrical conductivity, and electrocatalytic activities for oxygen reduction reaction. *Angew. Chem. Int. Ed.* **2016**, 55, 15301-15305.

(17) Yuan, B.; Li, C.; Guan, L.; Li, K.; Lin, Y. Prussian blue analog nanocubes tuning synthesis of coral-like Ni<sub>3</sub>S<sub>2</sub>@MIL-53(NiFeCo) core-shell nanowires array and boosting oxygen evolution reaction. *J. Power Sources* **2020**, 451, 227295.

- (18) Wu, Z.; Guo, J.; Wang, J.; Liu, R.; Xiao, W.; Xuan, C.; Xia, K.; Wang, D. Hierarchically porous electrocatalyst with vertically aligned defect-rich CoMoS nanosheets for the hydrogen evolution reaction in an alkaline medium. *ACS Appl. Mater. Interfaces* **2017**, *9*, 5288-5294.
- (19) Wang, Q.; Tian, Z.-Y.; Cui, W.-J.; Hu, N.; Zhang, S.-M.; Ma, Y.-Y.; Han, Z.-G. Hierarchical flower-like CoS<sub>2</sub>-MoS<sub>2</sub> heterostructure spheres as efficient bifunctional electrocatalyst for overall water splitting. *Int. J. Hydrog. Energy* **2022**, *47*, 12629-12641.
- (20) Liu, T.; Li, P.; Yao, N.; Kong, T.; Cheng, G.; Chen, S.; Luo, W. Self-sacrificial template-directed vapor-phase growth of MOF assemblies and surface vulcanization for efficient water splitting. *Adv. Mater.* **2019**, *31*, e1806672.
- (21) Xu, X.; Du, P.; Guo, T.; Zhao, B.; Wang, H.; Huang, M. In situ grown Ni phosphate@Ni<sub>2</sub>P<sub>5</sub> nanorod arrays as a unique core-shell architecture: competitive bifunctional electrocatalysts for urea electrolysis at large current densities. *ACS Sustain. Chem. Eng.* **2020**, *8*, 7463-7471.
- (22) Zhao, M.; Li, W.; Li, J.; Hu, W.; Li, C. M. Strong electronic interaction enhanced electrocatalysis of metal sulfide clusters embedded metal-organic framework ultrathin nanosheets toward highly efficient overall water splitting. *Adv. Sci.* **2020**, *7*, 2001965.
- (23) Feng, L. L.; Yu, G.; Wu, Y.; Li, G. D.; Li, H.; Sun, Y.; Asefa, T.; Chen, W.; Zou, X. High-index faceted Ni<sub>3</sub>S<sub>2</sub> nanosheet arrays as highly active and ultrastable electrocatalysts for water splitting. *J. Am. Chem. Soc.* **2015**, *137*, 14023-6.
- (24) Senthil Raja, D.; Lin, H.-W.; Lu, S.-Y. Synergistically well-mixed MOFs grown on nickel foam as highly efficient durable bifunctional electrocatalysts for overall water splitting at high current densities. *Nano Energy* **2019**, *57*, 1-13.
- (25) Hou, X.; Han, Z.; Xu, X.; Sarker, D.; Zhou, J.; Wu, M.; Liu, Z.; Huang, M.; Jiang, H. Controllable amorphization engineering on bimetallic metal-organic frameworks for ultrafast oxygen evolution reaction. *Chem. Eng. J.* **2021**, *418*, 129330.
- (26) Sun, F.; Wang, G.; Ding, Y.; Wang, C.; Yuan, B.; Lin, Y. NiFe-based metal-organic framework nanosheets directly supported on nickel foam acting as robust electrodes for electrochemical oxygen evolution reaction. *Adv. Energy Mater.* **2018**, *8*, 1800584.
- (27) Hou, X.; Zhou, J.; Xu, X.; Wang, X.; Zhang, S.; Wang, H.; Huang, M. Morphological modulation of CoFe-based metal organic frameworks for oxygen evolution reaction. *Catal. Commun.* **2022**, *165*, 106445.
- (28) Zhu, X.; Dai, J.; Li, L.; Zhao, D.; Wu, Z.; Tang, Z.; Ma, L.-J.; Chen, S. Hierarchical carbon microflowers supported defect-rich Co<sub>3</sub>S<sub>4</sub> nanoparticles: an efficient electrocatalyst for water splitting. *Carbon* **2020**, *160*, 133-144.
- (29) Chen, Y.; Zhang, X.; Qin, J.; Liu, R. Transition metal atom doped Ni<sub>3</sub>S<sub>2</sub> as efficient bifunctional electrocatalysts for overall water splitting: design strategy from DFT studies. *Mol. Catal.* **2021**, *516*, 111955.
- (30) Zhang, W.; Jia, Q.; Liang, H.; Cui, L.; Wei, D.; Liu, J. Iron doped Ni<sub>3</sub>S<sub>2</sub> nanorods directly grown on FeNi<sub>3</sub> foam as an efficient bifunctional catalyst for overall water splitting. *Chem. Eng. J.* **2020**, *396*, 125315.
- (31) Xu, Y.; Li, B.; Zheng, S.; Wu, P.; Zhan, J.; Xue, H.; Xu, Q.; Pang, H. Ultrathin two-dimensional cobalt-organic framework nanosheets for high-performance electrocatalytic oxygen evolution. *J. Mater. Chem. A* **2018**, *6*, 22070-22076.
- (32) Zhao, Z.; Shao, Q.; Xue, J.; Huang, B.; Niu, Z.; Gu, H.; Huang, X.; Lang, J. Multiple structural defects in ultrathin NiFe-LDH nanosheets synergistically and remarkably boost water oxidation reaction. *Nano Res.* **2021**, *15*, 310-316.
- (33) Zhou, C.; Chen, X.; Liu, S.; Han, Y.; Meng, H.; Jiang, Q.; Zhao, S.; Wei, F.; Sun, J.; Tan, T.; Zhang, R. Superdurable bifunctional oxygen electrocatalyst for high-performance zinc-air batteries. *J. Am. Chem. Soc.* **2022**, *144*, 2694-2704.
- (34) Wu, J.; Yu, Z.; Zhang, Y.; Niu, S.; Zhao, J.; Li, S.; Xu, P. Understanding the effect of second metal on CoM (M = Ni, Cu, Zn) metal-organic frameworks for electrocatalytic oxygen evolution reaction. *Small* **2021**, *17*, e2105150.
- (35) Wen, Q.; Yang, K.; Huang, D.; Cheng, G.; Ai, X.; Liu, Y.; Fang, J.; Li, H.; Yu, L.; Zhai, T. Schottky heterojunction nanosheet array achieving high-current-density oxygen evolution for industrial water splitting electrolyzers. *Adv. Energy Mater.* **2021**, *11*, 2102353.
- (36) Xu, H.; Fei, B.; Cai, G.; Ha, Y.; Liu, J.; Jia, H.; Zhang, J.; Liu, M.; Wu, R. Boronization-induced ultrathin 2D nanosheets with abundant crystalline-amorphous phase boundary supported on nickel foam toward efficient water splitting. *Adv. Energy Mater.* **2019**, *10*, 1902714.
- (37) Hu, N.; Du, J.; Ma, Y.-Y.; Cui, W.-J.; Yu, B.-R.; Han, Z.-G.; Li, Y.-G. Unravelling the role of polyoxovanadates in electrocatalytic water oxidation reaction: active species or precursors. *Appl. Surf. Sci.* **2021**, *540*, 148306.
- (38) Cheng, C.-C.; Cheng, P.-Y.; Huang, C.-L.; Raja, D.-S.; Wu, Y.-J.; Lu, S.-Y. Gold nanocrystal decorated trimetallic metal organic frameworks as high performance electrocatalysts for oxygen evolution reaction. *Appl. Catal. B: Environ.* **2021**, *286*, 119916.
- (39) Kumar, A.; Bui, V. Q.; Lee, J.; Jadhav, A. R.; Hwang, Y.; Kim, M. G.; Kawazoe, Y.; Lee, H. Modulating interfacial charge density of NiP<sub>2</sub>-FeP<sub>2</sub> via coupling with metallic Cu for accelerating alkaline hydrogen evolution. *ACS Energy Lett.* **2021**, *6*, 354-363.
- (40) Qi, L.; Su, Y.-Q.; Xu, Z.; Zhang, G.; Liu, K.; Liu, M.; Hensen, E. J. M.; Lin, R. Y.-Y. Hierarchical 2D yarn-ball like metal-organic framework NiFe(dobpdc) as bifunctional electrocatalyst for efficient overall electrocatalytic water splitting. *J. Mater. Chem. A* **2020**, *8*, 22974-22982.

Received: May 31, 2022

Accepted: July 1, 2022

Published online: July 8, 2022

Published: July 18, 2022